Three-dimensional harmonic holographic microcopy using nanoparticles as probes for cell imaging

Chia-Lung Hsieh,[1,2*] Rachel Grange,[1] Ye Pu,[1,2] and Demetri Psaltis[1,2]

[1]School of Engineering, EPFL, Station 17, 1015 Lausanne, Switzerland
[2]Department of Electrical Engineering, California Institute of Technology, 1200 East California Boulevard, MC 136-93, Pasadena, California 91125, USA
[*]Corresponding author: chia-lung.hsieh@epfl.ch

Abstract: Luminescent markers play a key role in imaging techniques for life science since they provide a contrast mechanism between signal and background. We describe a new type of marker using second harmonic generation (SHG) from noncentrosymmetric $BaTiO_3$ nanocrystals. These nanoparticles are attractive due to their stable, non-saturating and coherent signal with a femtosecond-scale response time and broad flexibility in the choice of excitation wavelength. We obtained monodispersed $BaTiO_3$ nanoparticles in colloidal suspensions by coating the particle surface with amine groups. We characterized the SHG efficiency of 90-nm $BaTiO_3$ particles experimentally and theoretically. Moreover, we use the coherent SHG signal from $BaTiO_3$ nanoparticles for three-dimensional (3D) imaging without scanning. We built a harmonic holographic (H^2) microscope which records digital holograms at the second harmonic frequency. For the first time, high-resolution 3D distributions of these SHG markers in mammalian cells are successfully captured and interpreted by the H^2 microscope.

References and links

1. B. A. Griffin, S. R. Adams, and R. Y. Tsien, "Specific covalent labeling of recombinant protein molecules inside live cells," Science **281**, 269-272 (1998).
2. M. Chalfie, Y. Tu, G. Euskirchen, W. W. Ward, and D. C. Prasher, "Green fluorescent protein as a marker for gene-expression," Science **263**, 802-805 (1994).
3. W. C. W. Chan, and S. M. Nie, "Quantum dot bioconjugates for ultrasensitive nonisotopic detection," Science **281**, 2016-2018 (1998).
4. A. Miyawaki, A. Sawano, and T. Kogure, "Lighting up cells: labelling proteins with fluorophores," Nature Cell Biol. **5**, S1-S7 (2003).
5. B. N. G. Giepmans, S. R. Adams, M. H. Ellisman, and R. Y. Tsien, "Review - The fluorescent toolbox for assessing protein location and function," Science **312**, 217-224 (2006).
6. R. M. Dickson, A. B. Cubitt, R. Y. Tsien, and W. E. Moerner, "On/off blinking and switching behaviour of single molecules of green fluorescent protein," Nature **388**, 355-358 (1997).
7. G. H. Patterson and D. W. Piston, "Photobleaching in two-photon excitation microscopy," Biophys. J. **78**, 2159-2162 (2000).
8. P. J. Campagnola and L. M. Loew, "Second-harmonic imaging microscopy for visualizing biomolecular arrays in cells, tissues and organisms," Nat Biotech **21**, 1356-1360 (2003).
9. P. J. Campagnola, M. D. Wei, A. Lewis, and L. M. Loew, "High-resolution nonlinear optical imaging of live cells by second harmonic generation," Biophys. J. **77**, 3341-3349 (1999).
10. Y. Pu, M. Centurion, and D. Psaltis, "Harmonic holography: a new holographic principle," Appl. Opt. **47**, A103-A110 (2008).
11. L. L. Xuan, S. Brasselet, F. Treussart, J. F. Roch, F. Marquier, D. Chauvat, S. Perruchas, C. Tard, and T. Gacoin, "Balanced homodyne detection of second-harmonic generation from isolated subwavelength emitters," Appl. Phys. Lett. **89**, 121118 (2006).

12. J. Chen, S. Machida, and Y. Yamamoto, "Simultaneous measurement of amplitude and phase in surface second-harmonic generation," Opt. Lett. **23**, 676-678 (1998).
13. S. Kluge, F. Budde, I. Dohnke, P. Rechsteiner, and J. Hulliger, "Phase-sensitive second-harmonic microscopy reveals polarity of topologically centrosymmetric molecular crystals," Appl. Phys. Lett. **81**, 247-249 (2002).
14. P. Marquet, B. Rappaz, P. J. Magistretti, E. Cuche, Y. Emery, T. Colomb, and C. Depeursinge, "Digital holographic microscopy: a noninvasive contrast imaging technique allowing quantitative visualization of living cells with subwavelength axial accuracy," Opt. Lett. **30**, 468-470 (2005).
15. B. W. Schilling, T. C. Poon, G. Indebetouw, B. Storrie, K. Shinoda, Y. Suzuki, and M. H. Wu, "Three-dimensional holographic fluorescence microscopy," Opt. Lett. **22**, 1506-1508 (1997).
16. J. Rosen, and G. Brooker, "Non-scanning motionless fluorescence three-dimensional holographic microscopy," Nat. Photonics **2**, 190-195 (2008).
17. A. V. Kachynski, A. N. Kuzmin, M. Nyk, I. Roy, and P. N. Prasad, "Zinc oxide nanocrystals for nonresonant nonlinear optical microscopy in biology and medicine," J. Phys. Chem. C **112**, 10721-10724 (2008).
18. J. C. Johnson, H. Q. Yan, R. D. Schaller, P. B. Petersen, P. D. Yang, and R. J. Saykally, "Near-field imaging of nonlinear optical mixing in single zinc oxide nanowires," Nano Lett. **2**, 279-283 (2002).
19. L. Bonacina, Y. Mugnier, F. Courvoisier, R. Le Dantec, J. Extermann, Y. Lambert, V. Boutou, C. Galez, and J. P. Wolf, "Polar Fe(IO3)(3) nanocrystals as local probes for nonlinear microscopy," Appl. Phys. B-Lasers Opt. **87**, 399-403 (2007).
20. Y. Nakayama, P. J. Pauzauskie, A. Radenovic, R. M. Onorato, R. J. Saykally, J. Liphardt, and P. D. Yang, "Tunable nanowire nonlinear optical probe," Nature **447**, 1098-1101 (2007).
21. N. Sandeau, L. Le Xuan, D. Chauvat, C. Zhou, J. F. Roch, and S. Brasselet, "Defocused imaging of second harmonic generation from a single nanocrystal," Opt. Express **15**, 16051-16060 (2007).
22. E. Delahaye, N. Tancrez, T. Yi, I. Ledoux, J. Zyss, S. Brasselet, and R. Clement, "Second harmonic generation from individual hybrid MnPS3-based nanoparticles investigated by nonlinear microscopy," Chem. Phys. Lett. **429**, 533-537 (2006).
23. P. Kim, S. C. Jones, P. J. Hotchkiss, J. N. Haddock, B. Kippelen, S. R. Marder, and J. W. Perry, "Phosphonic acid-modified barium titanate polymer nanocomposites with high permittivity and dielectric strength," Adv. Mater. **19**, 1001-1005 (2007).
24. B. Dubertret, P. Skourides, D. J. Norris, V. Noireaux, A. H. Brivanlou, and A. Libchaber, "In vivo imaging of quantum dots encapsulated in phospholipid micelles," Science **298**, 1759-1762 (2002).
25. S. Brasselet, V. Le Floc'h, F. Treussart, J. F. Roch, J. Zyss, E. Botzung-Appert, and A. Ibanez, "In situ diagnostics of the crystalline nature of single organic nanocrystals by nonlinear microscopy," Phys. Rev. Lett. **92**, 207401 (2004).
26. R. W. Boyd, *Nonlinear Optics*, Ch. 1 (Academic, New York, 1992), pp. 1-52.
27. D. R. Larson, W. R. Zipfel, R. M. Williams, S. W. Clark, M. P. Bruchez, F. W. Wise, and W. W. Webb, "Water-soluble quantum dots for multiphoton fluorescence imaging in vivo," Science **300**, 1434-1436 (2003).
28. A. A. Heikal, S. T. Hess, and W. W. Webb, "Multiphoton molecular spectroscopy and excited-state dynamics of enhanced green fluorescent protein (EGFP): acid-base specificity," Chem. Phys. **274**, 37-55 (2001).
29. M. A. Albota, C. Xu, and W. W. Webb, "Two-photon fluorescence excitation cross sections of biomolecular probes from 690 to 960 nm," Appl. Opt. **37**, 7352-7356 (1998).
30. L. Malmqvist and H. M. Hertz, "2nd-harmonic generation in optically trapped nonlinear particles with pulsed lasers," Appl. Opt. **34**, 3392-3397 (1995).
31. C. F. Bohren and D. R. Huffman, *Absorption and Scattering of Light by Small Particles*, (Wiley, 1998).
32. J. D. Jackson, *Classical Electrodynamics 3rd Ed.* Ch. 9 (Wiley, New York, 1998), p.412.
33. K. Konig, P. T. C. So, W. W. Mantulin, and E. Gratton, "Cellular response to near-infrared femtosecond laser pulses in two-photon microscopes," Opt. Lett. **22**, 135-136 (1997).
34. Y. Pu and H. Meng, "Intrinsic speckle noise in off-axis particle holography," J. Opt. Soc. Am. A-Opt. Image Sci. Vis. **21**, 1221-1230 (2004).
35. M. R. Lorenz, V. Holzapfel, A. Musyanovych, K. Nothelfer, P. Walther, H. Frank, K. Landfester, H. Schrezenmeier, and V. Mailander, "Uptake of functionalized, fluorescent-labeled polymeric particles in different cell lines and stem cells," Biomaterials **27**, 2820-2828 (2006).
36. M. Centurion, Y. Pu, and D. Psaltis, "Holographic capture of femtosecond pulse propagation," J. Appl. Phys. **100**, 063104 (2006).

Introduction

Fluorescent bio-markers such as organic dyes [1], green fluorescent protein (GFP) [2], and quantum dots (QDs) [3] have been popularly used for biomedical imaging due to their outstanding brightness and biocompatibility [4, 5]. We have developed a new type of marker using the SHG from noncentrosymmetric nanocrystals which we refer to as "Second

Harmonic Radiation IMaging Probes (SHRIMPs)". Due to the intrinsic properties of SHG, SHRIMPs emit a stable coherent signal which is suitable for long-term observations. These types of observations are usually complicated when using the fluorescent signal because of photobleaching and luminescence blinking [6, 7].

When a nanocrystal of noncentrosymmetric structure is optically excited at a fundamental frequency, it emits the optical signal at the exact doubled frequency. Only materials with crystalline structures lacking a center of symmetry are capable of efficient SHG. As a result, when imaged at the second harmonic frequency, SHRIMPs provide an effective mechanism of contrast between the markers and the generally unstructured or isotropic biological microenvironment. Ordered and highly polarizable biological noncentrosymmetric structures, such as the collagen fibers, have been known for endogenous SHG [8]. However, in most of the biological cell components, the endogenous SHG from the cell interface layers is weak [9].

Compared to fluorescent markers, SHRIMPs allow for significantly better imaging modalities due to their intrinsic properties. Unlike fluorescence, the process of SHG only involves virtual electron energy transition without nonradiative energy loss. Owing to this lossless, virtual transition process, SHRIMPs do not bleach over time and emit a stable, non-saturating signal with a femtosecond-scale response time. This allows for the observation of fast dynamic processes over a long time. Furthermore, SHG is generally a non-resonant process which offers the flexibility in the choice of excitation wavelength. This also results in the flexibility of tuning the wavelength of the SHG signal by changing the excitation wavelength accordingly. The coherent nature of the SHG signal is also a main advantage, providing a possibility to detect the second harmonic signal with interferometric optical techniques [10-13].

The principle of harmonic holography was recently demonstrated [10]. When the digital hologram is recorded at the doubled frequency, it captures both the amplitude and phase information of the SHG object field. Therefore the 3D field distribution, reflecting the 3D distribution of the SHRIMPs could be recorded without scanning. The spatial resolution is limited by the diffraction of light at the half wavelength, and the temporal resolution is limited by the laser pulse duration. Several holographic techniques have been developed for bio-imaging, for example the linear and fluorescent holographic microscopy [14-16]. H^2 microscopy is especially suitable for long-term imaging with luminescent markers due to the high imaging contrast provided by detecting the signal at SHG frequency: the background signal (linear background scattering and autofluorescence) can be efficiently removed by optical filters.

The SHG properties of several kinds of nanocrystals have been recently reported: ZnO [17, 18], $Fe(IO_3)_3$ [19], $KNbO_3$ [20], $KTiOPO_4$ (KTP) [11, 21] and SHG-active crystalline organic-inorganic hybrid nanoparticles [22]. Reference 22 reported the quantitative characterization of the SHG efficiency from nanocrystals both theoretically and experimentally. In this paper, we show the first quantitative characterization of SHG efficiency from $BaTiO_3$ nanocrystals. More generally, a theoretical model for the estimation of the absolute SHG power radiated from a single nanocrystal is described. We also report H^2 bioimaging with $BaTiO_3$ nanoparticles as SHRIMPs. We demonstrate the H^2 microscopy where for the first time the 3D distribution of SHRIMPs inside artificial samples and mammalian cells was recorded and reconstructed by one digital hologram.

1. Stabilization of the BaTiO₃ SHRIMPs in a colloidal suspension

The 30-nm and 90-nm $BaTiO_3$ nanoparticles were obtained commercially in dry powder from Nanoamor and Techpowder respectively. The X-ray diffraction measurement from the suppliers confirmed that the crystal structure is tetragonal, which is non-centrosymmetric, allowing for efficient SHG without any further treatment such as that described in reference 10. The dry $BaTiO_3$ nanoparticle powder was dispersed in 1.25 mM aminomethylphosphonic acid with the particle concentration of 10^{10} particles / cm^3. We treated the colloidal suspension

with ultrasound (Branson digital sonifier 450) for 10 minutes to break the clusters into individual particles. The suspension was then stirred for 24 hours. The phosphonic acid reacts and covers the particle surface [23] and it ends up with an amine group coated particle surface. The suspension is stabilized by electrostatic force from the ionization of the amine group in solution. Finally, we filtered out the big clusters from the suspension by flowing it through a membrane with pore size of 0.22 μm (Millipore Express PLUS). The surface charge of the stabilized particle is determined by the degree of ionization of the amine groups on the particle, which can be tuned by changing the pH of the solution. The zeta potential of the monodispersed colloidal suspension was obtained by light scattering measurement (Brookhaven Instruments Corp. ZetaPALS). We observed that the zeta potential decreases from 10 mV to -40 mV when the pH of the solution increases from 2 to 9. The amine group on the particle also offers many possibilities of crosslinking biomolecules such as proteins, antibodies, and DNAs for specific labeling [24].

We measured the 90-nm particle size distribution in suspension by dynamic light scattering (Brookhaven Instruments Corp. 90Plus) showing that most of the particles were well dispersed while less than 10% of the particles are clusters of double the size (Fig. 1). In the inset of Fig. 1, the scanning electron microscope image confirms the size of the particles which were dried on a conducting substrate.
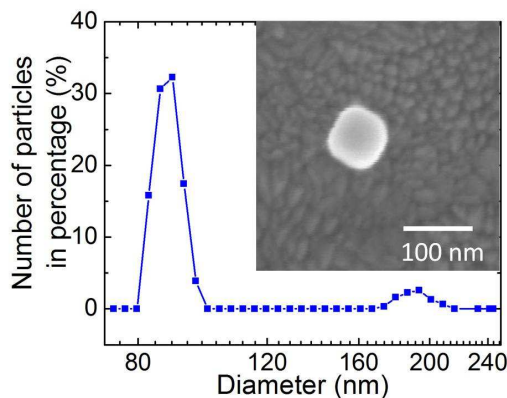

Fig. 1. Dynamic light scattering measurement of 90-nm BaTiO$_3$ particles colloidal suspension. Inset: Scanning electron microscope image of a single 90-nm BaTiO$_3$ particle.

2. Optical Characterization of the BaTiO$_3$ SHRIMPs

We measured the SHG efficiency by directly imaging BaTiO$_3$ nanoparticles. To perform the characterization, we deposited the nanoparticles on a glass substrate. The excitation light source consisted of 150 fs laser pulses centered at 800 nm wavelength (repetition rate 76 MHz) from a Ti:sapphire oscillator. The laser beam was slightly focused to reach the peak excitation intensity on the order of 1 GW/cm^2 on the sample. The SHG signal was collected by a 0.9 numerical aperture (NA) objective and imaged on an electron multiplying charge coupled device (EMCCD, Andor iXon^{EM}+ 885). We measured the power dependency and the optical spectrum to confirm the SHG signal (Fig. 2). The SHG signal was observed for an hour with less than 5 % decrease under continuous excitation.
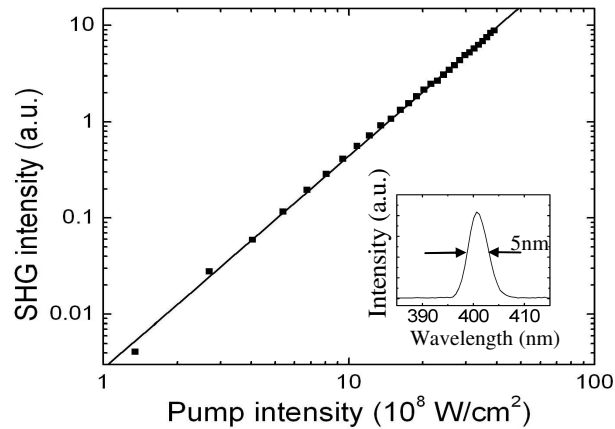
Fig. 2. Power dependence of the SHG signal from $BaTiO_3$ nanoparticles in double logarithmic scale. The squares are measured results and the solid line is the linear fit with the slope of 2.2. The inset shows the SHG optical spectrum centered at 400.6 nm with a full width half maximum of 5 nm.

We observed the polarization dependent SHG response from isolated nanocrystals by rotating the polarization of the excitation beam. The crystal orientation determines the polarization dependency of the SHG signal [25]. We chose the object with diffraction-limited SHG spot size for the measurement. An artificial frame is placed in Fig. 3 for ease of discussion: the sample plane is in the XY plane, the excitation laser propagates in the Z direction, and θ and ϕ are defined accordingly in Fig. 3. The direction of the excitation polarization can be described by ϕ. The measured SHG signals as a function of the angle of the excitation polarization are shown as circular dots in the polar diagram in Fig. 3. We simulated the polarization dependent SHG responses of a $BaTiO_3$ nanocrystal with the c-axis oriented at $\phi_0 = 90$ degree and $\theta_0 = 30, 50, 70, 90$ degree respectively. Due to the symmetry of the tetragonal crystal structure, the rotation of a $BaTiO_3$ nanocrystal respective to the c-axis does not change the SHG response. In the simulation, the SHG signal was calculated by using the second order susceptibilities of a bulk tetragonal $BaTiO_3$ crystal, where $d_{15} = -41 \times 10^{-9}$ esu, $d_{31} = -43 \times 10^{-9}$ esu, and $d_{33} = -16 \times 10^{-9}$ esu [26]. The simulation model is described in details later in this section. The simulated results show that the orientation of the nanocrystal determines the SHG polar response. When the c-axis tilts (θ_0 increases), the polar response changes the shape from a circle to a peanut-shape. When the c-axis rotates in the XY plane (ϕ_0 changes), the peanut-shape polar response rotates. It is worth noting that the orientation (regardless of the direction) of the c-axis of the nanocrystal cannot be uniquely determined from the polar diagram since there are ambiguities when $\phi = \phi_0$ and $\phi = \pi + \phi_0$. The simulated result of $\phi_0 = 90$ degree and $\theta_0 = 90$ degree matches with the experimental measurement, which implies the orientation of the nanocrystal under analysis is in the XY plane and is aligned in the Y axis direction. The match of the calculation with the measured results also shows that the object under analysis is either a single nanocrystal or a few nanocrystals with the same orientation. When nanocrystals are aligned, they behave the same as one nanocrystal in SHG response.
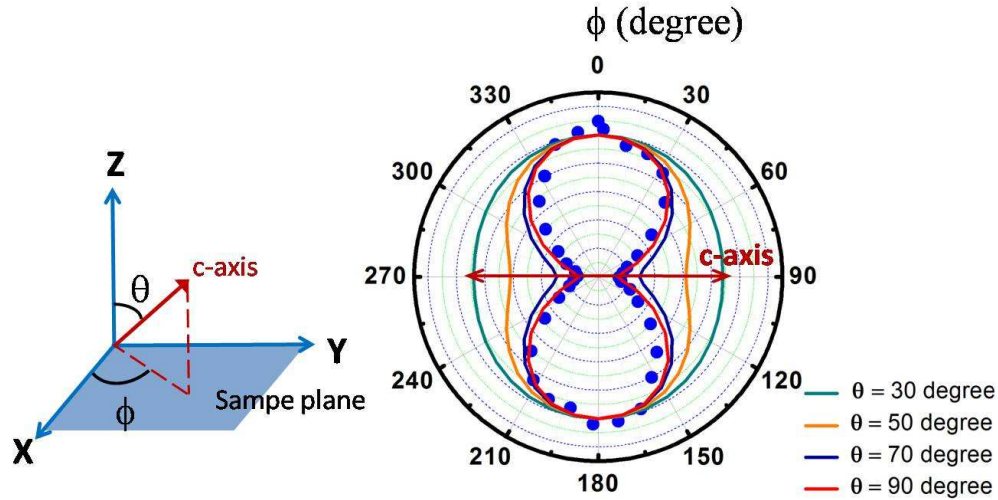
Fig. 3. Polarization dependent SHG response measured from an isolated BaTiO₃ nanocrystal. Dots: experimental data. Line: Theoretical calculation based on the second order susceptibility of a bulk BaTiO₃ crystal oriented at $\phi_0 = 90$ degree and $\theta_0 = 30, 50, 70, 90$ degree respectively. The red arrow in the polar diagram indicates the projection of the c-axis of the nanocrystal on the XY plane.

The absolute total SHG power emitted by the nanocrystal can be found by calibrating the collection efficiency of the optical system. The collection efficiency is the product of the collection ratio of the objective (determined by the solid angle of the numerical aperture), the transmission of the optical components at SHG frequency along the detection, and the quantum efficiency of the detector. The overall collection efficiency in our system was about 1%. Therefore the detected power is 1% of the total radiated SHG power (W_{2P}). To describe the brightness of SHRIMPs, we express W_{2P} by as follows:

$$W_{2P} = \sigma_{2P} \, I_{1P}^{\,2} \,. \tag{1}$$

where σ_{2P} is the two-photon cross section and I_{1P} is the excitation intensity. This has been the widely used expression for describing the brightness of two-photon fluorescent markers. SHG and two-photon fluorescence are both two-photon processes, but the mechanisms of the two processes are very different. SHG is a process without a real state transition. Therefore the σ_{2P} of a SHRIMP simply describes how efficient a SHRIMP can scatter at the SHG frequency under excitation at the fundamental frequency. On the other hand, two-photon fluorescence involves a two-photon absorption followed by a fluorescence emission. Therefore the two-photon (action) cross section σ_{2P} of two-photon fluorescent markers is the product of the two-photon absorption cross section and the fluorescent quantum efficiency. σ_{2P} is measured in unit of Goeppert-Mayer (1 GM = 10^{-50} cm⁴ sec photon⁻¹). From the polarization dependency measurement shown in Fig. 3, we obtained a σ_{2P} of the isolated BaTiO₃ nanoparticle in a range from 2,540 to 19,060 GM. As a reference, the σ_{2P} of the commonly used fluorescent bio-markers are listed: 47,000 GM for quantum dots [27], 75 GM for enhanced GFP [28], and 150 GM for Rhodamine 6G [29]. In general, the two-photon fluorescent efficiency depends strongly on the excitation wavelength due to the resonant absorption.

The SHG efficiency of a SHRIMP can be described with a model under the assumption that the SHRIMP is spherical [30]. The size of SHRIMPs in our study is much smaller than the excitation wavelength, so SHRIMPs can be thought as Rayleigh particles. When linearly

polarized electromagnetic waves excite SHRIMPs, the electric field inside the particles is in-phase and uniform as $E_1(\omega) = \left[3\varepsilon_2 / (\varepsilon_1 + 2\varepsilon_2)\right] E_2(\omega)$ [31], where $E_2(\omega)$ is the fundamental electric field in the surrounding medium and in absence of the particle, and ε_1 and ε_2 are the linear permittivities of the particle and the surrounding medium respectively. The electric field inside the particle will induce polarizations at the fundamental and harmonic frequencies through linear and nonlinear optical susceptibilities ($\chi^{(1)}, \chi^{(2)}, \cdots$). The total polarization is then expressed by a power series in the field strength $E_1(\omega)$ as:

$$P(\omega, 2\omega, \cdots) = \chi^{(1)} \cdot E_1(\omega) + \chi^{(2)} \cdot E_1(\omega) \cdot E_1(\omega) + \cdots. \qquad (2)$$

The polarization at the doubled frequency gives rise to SHG:

$$P(2\omega) = \chi^{(2)} \cdot E_1(\omega) \cdot E_1(\omega). \qquad (3)$$

The $P(2\omega)$ is thus in-phase and uniform inside the particle and it results in an induced dipole moment of the particle as $d(2\omega) = \left(4\pi a^3/3\right) P(2\omega)$ radiating like an antenna at the SHG frequency, where a is the radius of the particle. The total emitted power W_0 is the sum of the power radiated by the three dipole moment components $d_i(2\omega)$, $(i = x, y, z)$. We obtain [32]

$$W_0 = \frac{ck^4}{12\pi\varepsilon_0} \sum \left[d_i(2\omega)\right]^2, \qquad (4)$$

where c is the speed of light, k is the wave number at the SHG frequency, and ε_0 is the vacuum permittivity. Therefore one can calculate the power of the SHG signal emitted by a SHRIMP under certain excitation intensity. Following equation (1) and (4) with the $\chi^{(2)}$ of a bulk BaTiO$_3$ crystal, we can estimate the σ_{2P} of a SHRIMP of certain size, and vice versa. The model indicates that the size of the nanocrystal in the experiment shown in Fig. 3 was 95 nm, which is in the reasonable range as measured by dynamic light scattering. We calculate the σ_{2P} of a 90-nm BaTiO$_3$ SHRIMP as in a range from 1,735 to 13,010 GM. This range is due to the polarization dependent SHG response. The σ_{2P} is sensitive to the size of the particle, obeying the sixth-power dependency of the σ_{2P} on the radius of the particle. We estimate the σ_{2P} of 30-nm BaTiO$_3$ particles in a range from 3 to 20 GM under the assumption that the values of $\chi^{(2)}$ elements remain the same when the particle size decreases. This range is again the result of polarization dependent SHG response.

3. H^2 microscopy

We built a H^2 microscope to demonstrate the potential of SHRIMPs for scan-free 3D imaging. The excitation laser is the same as the one described previously. The peak intensity of the excitation is 1.5 GW/cm^2, which is 100 times less than the cell damage threshold [33] and is also 100 times less than that used in Ref. 10. The experimental setup is shown in Fig. 4. The H^2 microscope can be understood as a 4F imaging system followed by a holographic recording system. The SHG signal from SHRIMPs was collected and optically magnified 80 times by a 4F system consisting of a 0.9 NA microscope objective and a lens of 20 cm focal length. We put the EMCCD away from the 4F imaging plane so that the object field could propagate and fill the detection area of EMCCD. The hologram recording distance, i.e. the distance between the SHG image formed by the 4F system and the EMCCD, was 20 cm. A plane wave at doubled frequency generated by a separate β-barium borate (BBO) crystal served as the reference beam. The intensity ratio between the signal maximum and the reference beam is set to be 1:10. The signal and reference pulses were collinearly overlapping

both spatially and temporally on the EMCCD, and as a result an on-axis digital hologram was recorded at the SHG wavelength. The inherent twin image has little effect on reconstructed image due to the long hologram recording distance. The algorithm of holographic reconstruction is described in Ref. 10.
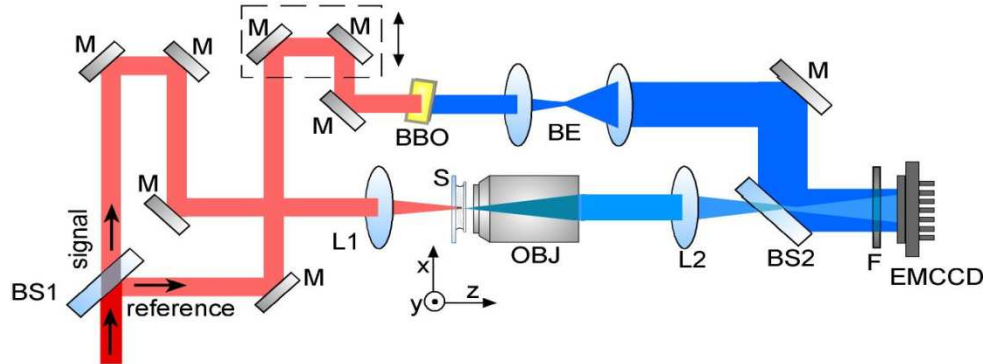

Fig. 4. H^2 microscope experimental setup. BS1 and BS2, beam splitters; M, mirror; L1 and L2, lens; S, sample; OBJ, microscope objective; BE, beam expander; F, band-pass filter centered at 400 nm. BS1 splits the laser into signal and reference beams. In the signal arm, L1 slightly focuses the excitation beam into the sample with SHRIMPs. OBJ and L2 form a 4F imaging system to collect and optically magnify the SHG image of SHRIMP. The EMCCD is placed away from the 4F imaging plane. A band-pass filter is placed in front of the EMCCD to remove the excitation from the SHG signal. The reference beam goes through a translation stage and a BBO crystal so that the coherent reference SHG laser pulses are generated and can be temporally and spatially overlapped with the signal on the EMCCD. The signal and reference beams are combined collinearly by BS2 and therefore an on-axis digital hologram is recorded on the EMCCD.

4.   Single SHRIMP detection with the H^2 microscope

The H^2 microscope was sensitive enough to image an isolated $BaTiO_3$ nanocrystal. Since the particle size is smaller than the optical diffraction limit at the SHG wavelength, the image of a single particle reflects the spatial resolution of the H^2 microscope. The nanocrystal to be imaged was the same nanocrystal characterized in the polarization dependent measurement as shown in Fig. 3. Figure 5 (a) shows the focused SHG image of the $BaTiO_3$ particle taken by the conventional 4F imaging system. The spot size is 0.4 μm which is the diffraction limit. We then imaged the same particle with the H^2 microscope. The single particle behaved as a point source at the SHG frequency. The radiated spherical waves interfered with the reference plane waves and a set of interference rings (Fresnel zone plates) were formed and recorded on the detector plane. By digital propagation, we can reconstruct the field at any plane from the recorded Fresnel zone plates. Figure 5 (b) is the harmonic holographic reconstructed image of the same $BaTiO_3$ particle on the object plane, which shows the same spot size as the Fig. 5 (a). Therefore, the H^2 microscope has diffraction-limited resolution. The axial resolution of the H^2 microscope can be measured by digital holographic reconstruction of a stack of images along the axial direction. The measured axial resolution was about 2 μm as shown in Fig. 5 (c). The axial resolution may be improved by calibrating the aberration introduced by the optics for the signal collection, especially the spherical aberration introduced by the objective.
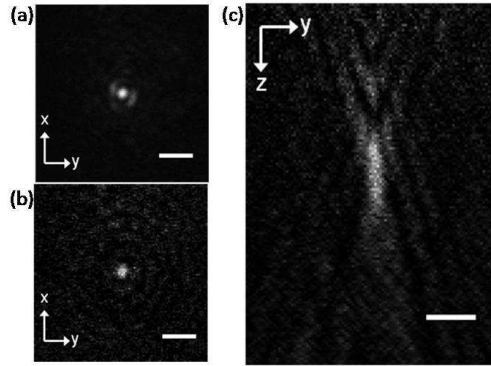
Fig. 5. Spatial resolution of the H^2 microscope measured by imaging an isolated BaTiO$_3$ particle. (a) SHG intensity image measured by a conventional microscope. (b) Holographic reconstructed intensity image at the object plane. (c) Cross section of a stack of holographic reconstructed intensity images along the axial direction. The scale bars are 2 μm.

5. H^2 microscopic 3D imaging

The capability of the H^2 microscope for 3D SHRIMP imaging was first evaluated by imaging an artificial 3D sample. We prepared a 3D distribution of SHRIMPs by randomly embedding 30-nm BaTiO$_3$ nanoparticles in a ~100-μm thick polydimethylsiloxane (PDMS) film. The SHRIMPs were immobilized inside the film when the PDMS was cured. Figure 6 (a)-(d) show the conventional SHG microscope images of four sub-micron BaTiO$_3$ clusters on four different planes under excitation. These four clusters were then imaged by the H^2 microscope. The results are shown in Fig. 6 (e)-(h). We changed the focus by digitally reconstructing the images at different planes. The relative depths of the reconstructed planes were 0, 9.4, 17.2, and 20.3 μm respectively. The reconstructed images in Fig. 6 (e)-(h) agree well with the SHG images in Fig. 6 (a)-(d), suggesting that 3D distributions of SHRIMPs can be reliably recorded and interpreted from a single digital hologram without scanning. It is worth noting that the H^2 microscopy would have difficulty imaging a high density of SHRIMPs [34]. This difficulty results from the intrinsic speckle noise and it is a fundamental limit of storing 3D information with a 2D image. However, when the density of SHRIMPs is low, the H^2 microscopy with SHRIMPs makes scan-free 3D imaging possible.
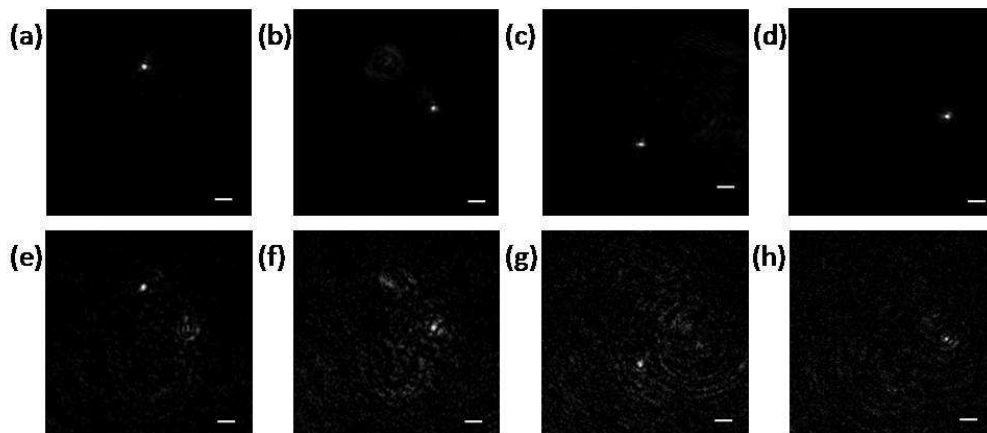

Fig. 6. Images of SHRIMPs embedded in PDMS. (a)-(d): SHG images of SHRIMPs on four different planes, focusing by moving the optics with a conventional microscope. (e)-(h): Holographic reconstructed images of SHRIMPs on four corresponding planes, focusing by digital reconstruction. The relative depths of these four planes are 0, 9.4, 17.2, and 20.3 μm respectively. Scale bars are 2 μm.

6. 3D imaging of the SHRIMPs in HeLa cells

SHRIMPs make scan-free 3D bio-imaging possible when they are labeled on the targets of interest and imaged with the H^2 microscope. Here we demonstrate the capability of the H^2 microscopy with SHRIMPs for 3D bio-imaging, as well as the biocompatibility of $BaTiO_3$ nanoparticles as SHRIMPs. The sample under analysis was mammalian (HeLa) cells non-specifically labeled with SHRIMPs. HeLa cells were incubated for 24 hours at 37 °C with 30-nm $BaTiO_3$ particles that have been stabilized with aminomethylphosphonic acid. During the incubation, the amine group present on the SHRIMPs surface encouraged the cells to uptake them through endocytosis [35]. SHRIMPs would be engulfed non-specifically into vesicles and packed as clusters randomly by the cells. In this way a 3D distribution of SHRIMPs was formed inside the cells. Cross section views of a cell imaged by a confocal scanning microscope (Leica, SP5) shown in Fig. 7 confirms that the SHRIMPs entered the cells by endocytosis. After 24-hour incubation, the HeLa cells were still alive.
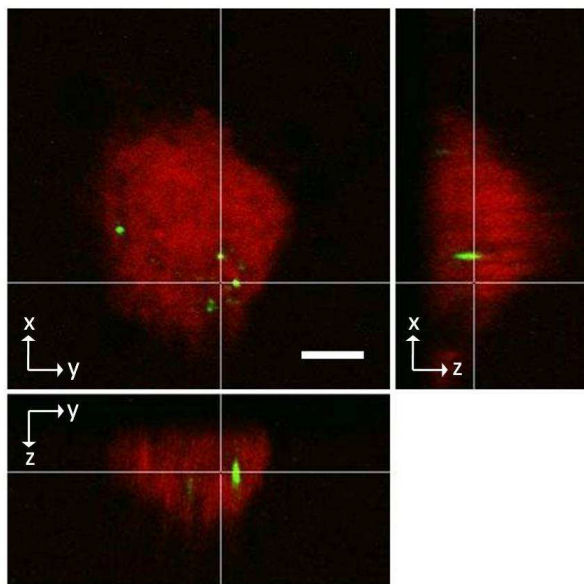

Fig. 7. Confocal section images of a calcein-stained HeLa cell (in red) with SHRIMPs (in green) inside it. The excitation consisted of femtosecond laser pulses centered at 800-nm wavelength. Calcein emits two-photon fluorescence signal (in red) while SHRIMPs emit SHG signal (in green). It is clear that the SHRIMPs entered the cell through endocytosis. The scale bar is 5μm.

We washed away the unbound SHRIMPs with a buffer solution (phosphate buffered saline, PBS) and fixed the cells with 3.7% parafolmaldehyde. The sample was then ready to be holographically imaged. Figure 8 (a) shows the superposition of the bright field transmission image of a cell and the SHG image from SHRIMPs taken by a conventional microscope. In Fig. 8 (a), we observed some SHRIMPs appeared as bright spots because they were on focus, while the others were not visible because they were out of focus. We assign the SHRIMPs in Fig. 8 (a) with unique numbers for ease of discussion. We imaged the same area with the H^2 microscope. By digital reconstruction, we observed that several SHRIMPs appeared on different planes. Figure 8 (b)-(d) show the reconstructed images on three different depths of the cell (0, 3.12, and 6.24 μm) where different clusters got on focus respectively. Since the cells uptook the SHRIMPs randomly, the size of the SHRIMP clusters, and therefore the SHG intensity, varied in a wide range (about a factor of 10). We see strong signal from the cluster number 4 both on the depths of 0 and 3.12 μm because it is a big cluster. Figure 8 (e) shows the normalized line intensity profiles of the six clusters when they

are on focus through digital reconstruction. All of them show a high signal to noise ratio. The cluster number 3 has a weak signal, and in its line intensity profile we can see the defocused signal from the cluster number 4. The acquisition time of the digital hologram was 1 minute, limited by the integration time for detectable signal. The acquisition time can be further optimized by increasing the excitation power and also the sensitivity of the detection. The peak intensity used in the experiment was 100 times weaker than the critical intensity affecting the cellular metabolism [33], so there is a room to further increase the pump intensity, and, as a result, the SHG signal intensity. The collection efficiency of the SHG signal was ~1%, which could also be significantly improved by adapting the optics for the SHG frequency. Moreover, the reference beam in holography can serve as a coherent local oscillator, leading to a gain in signal to noise ratio and a shot noise-limited performance of detection even at fast read-out [10]. As a pulsed holographic technique, the H^2 microscopy could reach a temporal resolution limited by the laser pulse width [10, 36].
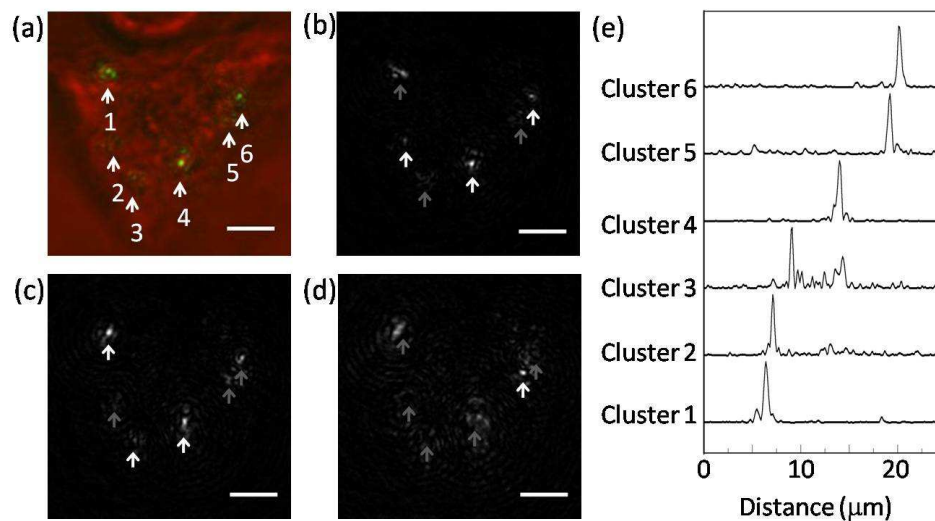

Fig. 8. Images of SHRIMPs non-specifically labeling HeLa cells (a) Superposition of the bright field transmission image of a HeLa cell (in red) and the SHG image of SHRIMPs (in green) taken by a conventional microscope. Six SHRIMPs clusters assigned with numbers were under analysis. Some of them cannot be seen clearly because they are out of focus. (b)-(d) H^2 reconstructed images at three different planes with relative depths of 0 μm, 3.12 μm and 6.24 μm respectively. The white arrows show the SHRIMPs that are on focus, while the gray arrows show the SHRIMPs that are out of focus. The SHRIMP labeled with number 4 is a big cluster so that it is bright both in (b) and (c). (e) Normalized intensity line profiles of the six clusters when they are on focus through digital reconstruction. The scale bars are 5 μm.

7. Conclusion

We have demonstrated the H^2 microscopy with $BaTiO_3$ nanoparticles as SHRIMPs for high-resolution 3D imaging. The coherent SHG signal from SHRIMPs allows us to capture the 3D distribution of these markers in specimens by a H^2 microscope without scanning. SHRIMPs possess several unique properties, including long-term observation without photobleaching, flexibility in excitation wavelength, coherent signals for 3D imaging, and ultrafast response time. In general, SHRIMPs are not replacements for fluorescent markers such as GFPs or QDs. Instead they provide new modalities of imaging applications. The $BaTiO_3$ nanoparticles were stabilized in colloidal suspension by electrostatic repulsion force through ionization of the amine group present on the surface of the particle. A stable suspension of narrow particle

size distribution was obtained. The amine group present on the particle surface also offers the general crosslink for further conjugation to proteins or antibodies for specific labeling. The quantitative polarization dependent SHG response of SHRIMPs was characterized experimentally and theoretically. By dynamically measuring the polarization dependence of the SHG response, we could track the orientation of a SHRIMP. As a result, not only the displacement but also the rotation of a SHRIMP could be monitored in the far field, which completes the detection schemes of SHRIMPs as imaging markers. Taking advantage of the coherent signal of SHRIMPs, we demonstrated the H^2 microscope as a 3D imaging technique. For the first time, the 3D distributions of SHRIMPs in biological specimens were imaged by the H^2 microscope with diffraction limited spatial resolution.